UPCommons

Portal del obert de la UPC

1   **Interaction of Saturn's Hexagon with convective storms**

2

3   **A. Sánchez-Lavega[1,*], E. García-Melendo[2], T. del Río-Gaztelurrutia[1], R. Hueso[1], A. Simon[3], M.H.**
4   **Wong[4], K. Ahrens-Velásquez [2], M. Soria[2], T. Barry[5], C. Go[6], C. Foster[7]**

5

6   [1] Departamento Física Aplicada I, Escuela de Ingeniería de Bilbao, Universidad del País Vasco
7   UPV/EHU, Bilbao, Spain.

8

9   [2] Universitat Politècnica de Catalunya UPC, Terrasa, Spain

10

11   [3] NASA Goddard Space Flight Center/690, Greenbelt, MD, USA

12

13   [4] University of California, Berkeley, CA, USA

14

15   [5] Broken Hill Observatory, Broken Hill, Australia

16

17   [6] University of San Carlos, Cebu, Philippines

18

19   [7] Astronomical Society of Southern Africa, Centurion, South Africa

20

21   Corresponding author: Agustín Sánchez-Lavega (agustin.sanchez@ehu.eus)

22

23   **Key Points:**

24

- Following an outbreak of polar storms in 2018, we observed in March-May 2020 a new
  episode of storms south of Saturn's hexagonal wave.

- The storms did not produce a noticeable change in the zonal wind profile in the polar
  area.

- The hexagon shape was perturbed after the storms but the wave suffered no change in
  its rotation period matching that of System III.

Abstract

In March 2020 a convective storm erupted at planetographic latitude 76°N in the southern flank of Saturn's long-lived hexagonal wave. The storm reached a zonal size of 4,500 km and developed a tail extending zonally 33,000 km. Two new short-lived storms erupted in May in the hexagon edge. These storms formed after the convective storms that took place in 2018 in nearby latitudes. There were no noticeable changes in the zonal profile of Saturn's polar winds in 2018-2020. Measurements of the longitude position of the vertices of the hexagon throughout this period yield a value for its period of rotation equal to that of System III of radio-rotation measured at the time of Voyagers. We report changes in the hexagon clouds related to the activity of the storms. Our study reinforces the idea that Saturn's hexagon is a well rooted structure with a possible direct relationship with the bulk rotation of the planet.

Plain Language

Convective storms of zonal extents greater than 4,000 km are rare in Saturn's atmosphere. They occur every few years, and exceptionally, (perhaps once every 20-30 years) they reach 10,000 km and become a Great White Spot that expands along an entire latitudinal band of the planet. In 2018, multiple eruptions of medium-sized storms occurred close to the North Polar Region. After a period of calm throughout 2019, new eruptions took place in 2020, at 76°N latitude on the border of the hexagon wave, the closest to the pole ever observed. These storms changed the morphology of the clouds in the region, but the hexagon itself was not affected in its motion or dynamics, with no change in the zonal winds. This, together with its longevity, indicates that the hexagon is a robust meteorological formation. Its rotation period in these years remained that of the System III radio rotation measured by the Voyager spacecraft, reinforcing the idea of its possible direct relationship with the bulk rotation of the planet.

1 Introduction

From March to August 2018 four outbreaks of convective storms took place sequentially at planetographic latitudes from 66.7°N to 74.7°N, disturbing a whole latitude band spanning a width of ~ 8,000 km [Sánchez-Lavega et al., 2020]. Subsequently and throughout 2019, no new storms occurred, although the entire region between latitudes 66ºN and 75ºN presented numerous spots and white and dark areas (in visible wavelengths) difficult to track due to their low contrast and variability in short time scales (Figure S1). On March 25, 2020, a new convective outbreak started with a sudden bright spot (Figure 1) northwards of the 2018 events, on the edge of Saturn's hexagonal wave at 79°N where the wind profile turns anticyclonic [Sánchez-Lavega et al., 2014; Antuñano et al., 2015; Sayanagi et al., 2019]. Later in May of 2020, two other short-lived storms emerged, this time even further north on the southern flank of the hexagon. Two aspects of this phenomenon are of interest. On one hand, the convective storms themselves, due to their size and brightness (and energy involved), have never been reported before at polar latitudes in Saturn. On the other hand, their location next to the hexagon, which allows the study of their interaction with this enduring wave, provides new information about the hexagon itself,

79 in particular regarding its stability, robustness and longevity when subjected to nearby severe
80 disturbances. Finally, we explore if the extensive and intense convective activity in 2018 and 2020
81 had an effect on Saturn's zonal wind profile at these latitudes.
82
83 **2 Observations**
84
85 For this study we used two sets of data: (1) Images obtained using the "lucky imaging"
86 methodology in the spectral range 380-950 nm by a large number of observers distributed
87 around the world using telescopes of 30-50 cm in diameter (see Supporting Information). These
88 images provide a continuous survey with a nearly daily coverage of Saturn during the apparitions
89 in the years 2018 (from 23 March to 21 November, opposition 27 June), 2019 (from 27 February
90 to 28 October, opposition 9 July) and 2020 (25 March – 10 October, opposition 20 July). In total,
91 we navigated and measured about ~ 560 images selected among the ~ 3,000 images for years
92 2019-2020 submitted to the PVOL image database [Hueso et al., 2018] and to the ALPO-Japan
93 web site (see Supporting Information). Most images are either color RGB composites or red- to
94 near-infrared images in the wavelength ranges ~ 650-950 nm and 750-950 nm. They have a
95 spatial resolution ~ 600 – 900 km in the disk under the best seeing conditions; (2) Hubble Space
96 Telescope (HST) images obtained as part of the OPAL program [Simon et al., 2015] in one visit
97 per year close to the opposition (6-7 June 2018, 19-20 June 2019, 4-5 July 2020). These images
98 were obtained with the Wide Field Camera 3 (WFC3) using filters F225W, F275W, F343N, F395N,
99 F467M, F502N, F631N, F658N, FQ727N (methane absorption band), F763M, and FQ889N
100 (methane absorption band). Details of the image analysis is given in [Sánchez-Lavega et al., 2020]
101 and in Supporting Information.
102
103
104

105
106
107
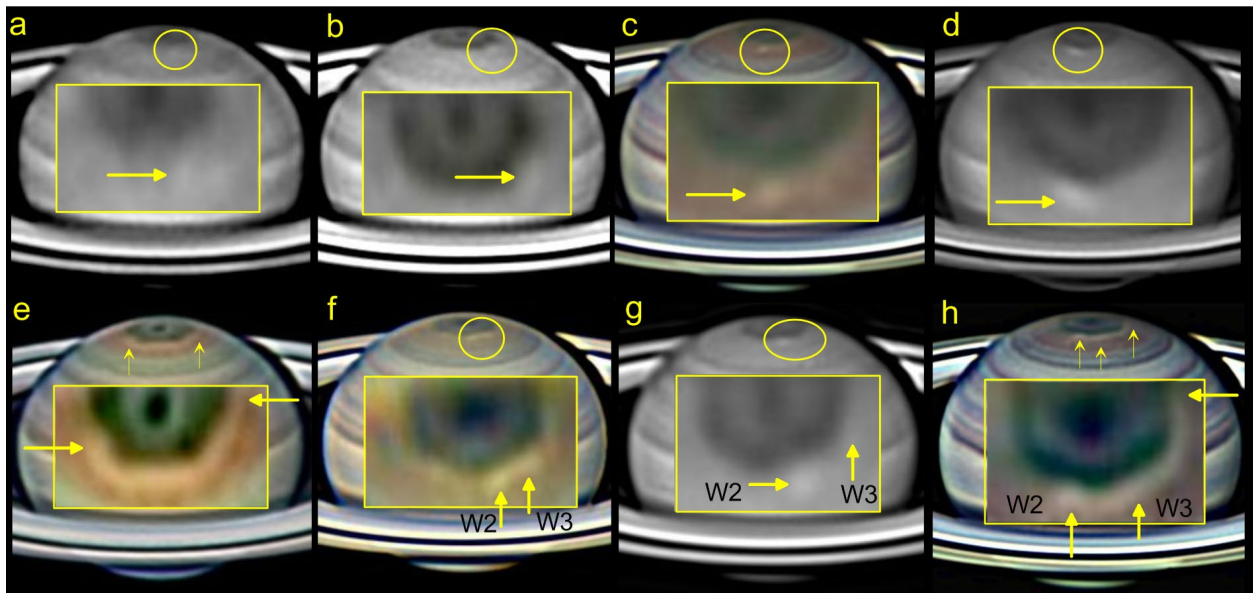
Figure 1. *Ground-based images of the convective storms in 2020. The storms are identified on the disk by circles and arrows to indicate their zonal expansion. The inset shows a polar projection of the storms and the hexagon. Storm W1 is visible in (a) March 25, red, C. Foster; (b) March 29, red, C. Foster; (c) April 11, RGB, C. Go; (d) April 12, red, N. MacNeill; (e) April 15, RGB, D. Peach, where the storm expands eastward. Storms W2 and W3 are shown in (f) May 1, RGB, T. Oliveti; (g) May 3, red, M. L. G. Wong; (h) May 5, RGB, C. Go, with storm W3 expanding eastward.*

3. Storm activity and the zonal wind profile

The first polar storm of 2020 (W1) was captured on March 25 2020 at latitude 74°N at red wavelengths as a faint bright spot ~ 4,000 km wide (Figure 1a). The following days the spot kept the same aspect (Figure 1b-c), and 4 days after outbreak, on March 29, it had expanded zonally, forming a tail that by April 11 reached ~ 17,000 km east of its head (Fig. 1d). We interpret this tail as the expansion of the storm clouds by winds blowing eastward relative to the actively-convecting plume-head with a velocity of 11 ms^{-1} (or 3.3 ms^{-1} in System III). In April 15 the storm head had a size of 5,400 ± 500 km, penetrating into the hexagon up to latitude 79.5°N (or 1,270 km into the south side of the hexagon) (Figure 1e). At that date, the tail of white clouds surrounded the hexagon, extending at least 39,200 km east of the head. This implies an eastward expansion by the winds relative to the head with a velocity of 21 ms^{-1} (or 14 ms^{-1} in System III). Figure 2a shows our measurements of the drift of the head of the storm in System III longitude and in Table 1 we give the velocity values, which fit well Saturn's wind profile at these latitudes [Sánchez-Lavega et al., 2000; García-Melendo et al., 2011]. Figure 2b shows that W1 migrated ~ 2.3° (~ 2,600 km) northwards of its onset position, towards the hexagon edge. The meridional velocity resulting from a linear fit to this drift was +1.2 ms^{-1}.

On May 1, two other bright spots (W2 and W3) were detected (Figure 1f-g-h). We consider them as new outbreaks arising in the expanding tail of the main storm W1, which was no longer visible on this date. The onset of W2 took place 2,250 km east of the expected position of W1, and W3 emerged 9,250 km further east of W2 (Figure 1f). Both spots were located northward by 0.7° of W1 and moved faster, (Figure 2a and Table 1) in agreement with the wind profile (Figure 2c). They were located on the anticyclonic side of the eastward jet embedded in the hexagon, thus interacting with it. From May 3 to August 1 we detected about 40 diffuse white spots at latitudes 75.5°N - 77°N, close to the hexagon (Fig. 2a, Fig. S2). Except for an isolated dark spot DS (figure 3b) at 76.6°N (u = 25 ms^{-1}), the variability and low contrast of these spots makes their identification and tracking difficult, so we did not try to measure their velocities. However their presence indicates that the activity continued on the south side of the hexagon for months after the three main storm outbreaks.

In order to see if this stormy activity had any influence on the zonal wind profile, we measured the motions of cloud features in the years of interest using different methods. First, we measured the winds in pairs of images from the HST OPAL program separated by one rotation of the planet, using the image correlation velocimetry technique [Hueso et al., 2009, Sánchez-Lavega et al., 2019]. The images selected were obtained in red filters (F631N, F763N) where the contrast of the cloud features is highest. This profile was binned in boxes of 0.5° width in latitude

152   giving velocity errors of 15 ms^{-1} (Simon et al., 2021). Secondly, we performed a manual tracking
153   of the most significant features in the stormy region using 4-5 HST images with a maximum
154   coverage over time ($\sim 10 - 14$ hr), giving velocity measurements with errors < 10 ms^{-1}. Finally, we
155   tracked the most prominent features from ground-based images, a technique that provides very
156   accurate velocities due to the long temporal coverage (errors ~ 1 ms^{-1}, Fig. S3-S4). In this last
157   case, most of the features correspond to spots in the double jet between 60ºN and 65ºN where
158   cyclones and anticyclones tend to concentrate [del Rio-Gaztelurrutia et al., 2018]. Their long term
159   track in 2020 is shown in Fig. 2a, 2b and S3 and the resulting wind profile is shown in Figure 2c.
160   The long-term track of this kind of spot in 2019 (Fig. S4) and the similarly derived wind profile for
161   that year are shown in Fig. S4 and S5). A comparison with the velocity profiles measured in 1981
162   using Voyager images [Sánchez-Lavega et al., 2000] and in 2004-2009 using Cassini images
163   [García-Melendo et al. 2011] indicates that within measurement uncertainties, the wind profile
164   was not affected by the storm activity, confirming our previous results for 2018 [Sánchez-Lavega
165   et al., 2020].
166
167   **TABLE 1**
168   **Motions of the convective storms and Hexagon wave vertices**
169

Feature	Onset (2020)	Latitude $\varphi(°)$	Drift ω (°d^{-1})	Zonal velocity u (ms^{-1})	Tracking time (d)
W1	25 March	75.6° ± 1°	2.32	-7.7	36
W2	1 May	76.3° ± 0.5°	-7.8	24.8	5
W3	1 May	76.3° ± 0.7°	-8.9	28.7	5
Hexagon 2018	29 Mar – 3 Nov	78.4° ± 0.3°	+0.017 ± 0.024	-0.046 ± 0.065	219
Hexagon 2019	7 Apr – 28 Oct	78.4° ± 0.3°	-0.0095 ± 0.018	+0.026 ± 0.065	204
Hexagon 2020	26 Mar - 20 Nov	78.4° ± 0.3°	-0.008 ± 0.010	+0.026 ± 0.063	229

170
171
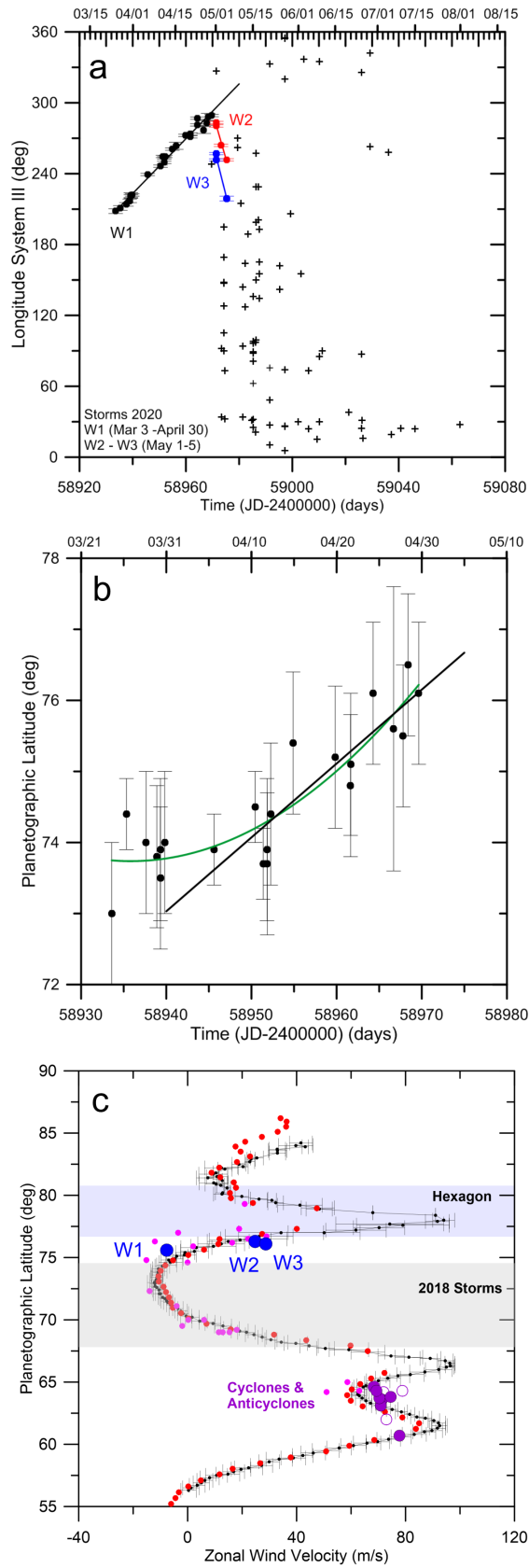
174 **Figure 2***. Motions and velocities of the convective storms in 2020. (a) Drift in System III longitude
175 of storms W1, W2, W3 between 25 March and 5 May 2020. Other smaller and low-contrast spots
176 in the latitude range 74°N-76.5°N are identified by crosses (Fig. S2); (b) Drift in planetographic
177 latitude of the center of storm W1. The green line corresponds to a degree-two polynomial fit and
178 the black line to a linear fit. In (a) and (b) the date (month/day) is indicated in the upper axis (c)
179 Zonal wind profile in Saturn's North Polar Region in 2020 relative to System III rotation frame. The
180 red dots are from the correlation velocimetry on HST images (Simon et al., 2021) and magenta
181 dots from major selected features from manual tracking on the same images. The three blue dots
182 identified as W1, W2 and W3 correspond to the three storms. The purple disks and circles are
183 from the tracking of long-lived spots in ground-based images (Fig. S3). The black line and dark
184 dots correspond to the reference wind profile from Cassini ISS measurements [García-Melendo et
185 al., 2011]. The gray areas indicate the latitude band where the 2018 storms evolved and the
186 location of the hexagon.*
187
188 **4. The Hexagon wave**
189
190 The presence of convective storms on the southern flank of the hexagon, and their
191 resulting interaction with it, provides a good test to probe the effects of storms on the wave. In
192 Figure 3, we show composite maps of the polar region using HST OPAL images from years 2018-
193 2020, at a wavelength of 763 nm where the hexagon is usually well contrasted. The vertices of
194 the hexagon are identified as V1 to V6 in Figure 4. In the period 2018-2020 the hexagon clouds
195 [Sanz-Requena et al., 2018] showed changes with respect to their usual sinusoidal distribution
196 [Antuñano et al., 2015]. The eastward jet embedded on the hexagon has peak velocities at 78.3°N
197 and it is usually traced at 763 nm by white clouds, surrounded on the north and south by low
198 albedo belts of varied contrast at ~ 76.5°N and 80.5°N [Antuñano et al. 2015, 2018, Sayanagi et
199 al., 2018]. In 2018 the northern belt and a white zone were very prominent (Fig. 3a), with the
200 transition between them near the peak of the jet. However, in 2019, there was a strong contrast
201 drop in these bands and the hexagon was visible by contrast at the equatorial edge of the
202 northern belt (Figure 3c-d) at about 78.6°N. A faint white zone and a hint of a darker belt are
203 visible south of it. Dark features moving rapidly at the edge of the hexagon changed its regular
204 aspect and made identification of vertices difficult (Fig. 3c-d). These features moved with the
205 hexagon eastward jet (Fig. S5). Finally, in 2020 the contrast was recovered, highlighting the two
206 belts enclosing the white band (Fig. 3b). It is tempting to correlate these changes in the clouds
207 with the storm activity in 2018 and 2020.
208
209
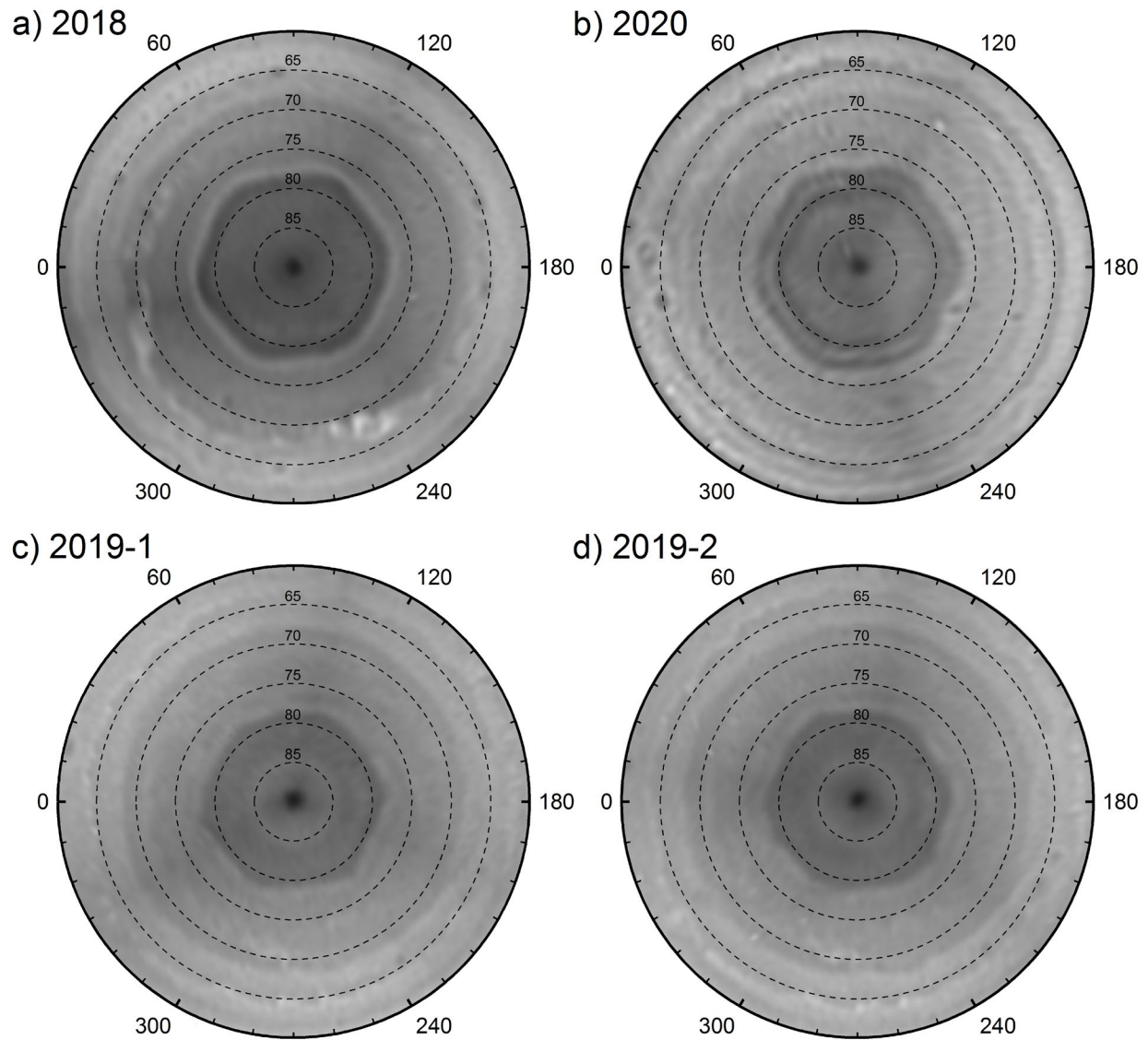
Figure 3. The hexagonal wave from HST images. Composite polar map projections of 763nm images for the following dates: (a) 6 June 2018 9:54; 6:43 and 12:49 ; (b) 4 July 2020 21:13 and 5 July 2020 0:24 and 3:35 (c) 20 June 2019 00:09; 03:27 and 06:38 (d) 20 June 2019 08:06; 11:16; 14:24 and 17:34. Vertices V1 to V6 are at approximate System III longitudes 60°, 120°, 180°, 240° 300° and 360°. Spot DS can be identified in (b) at longitude 200° and latitude 76.6°. Planetographic latitudes are indicated by dashed circles.
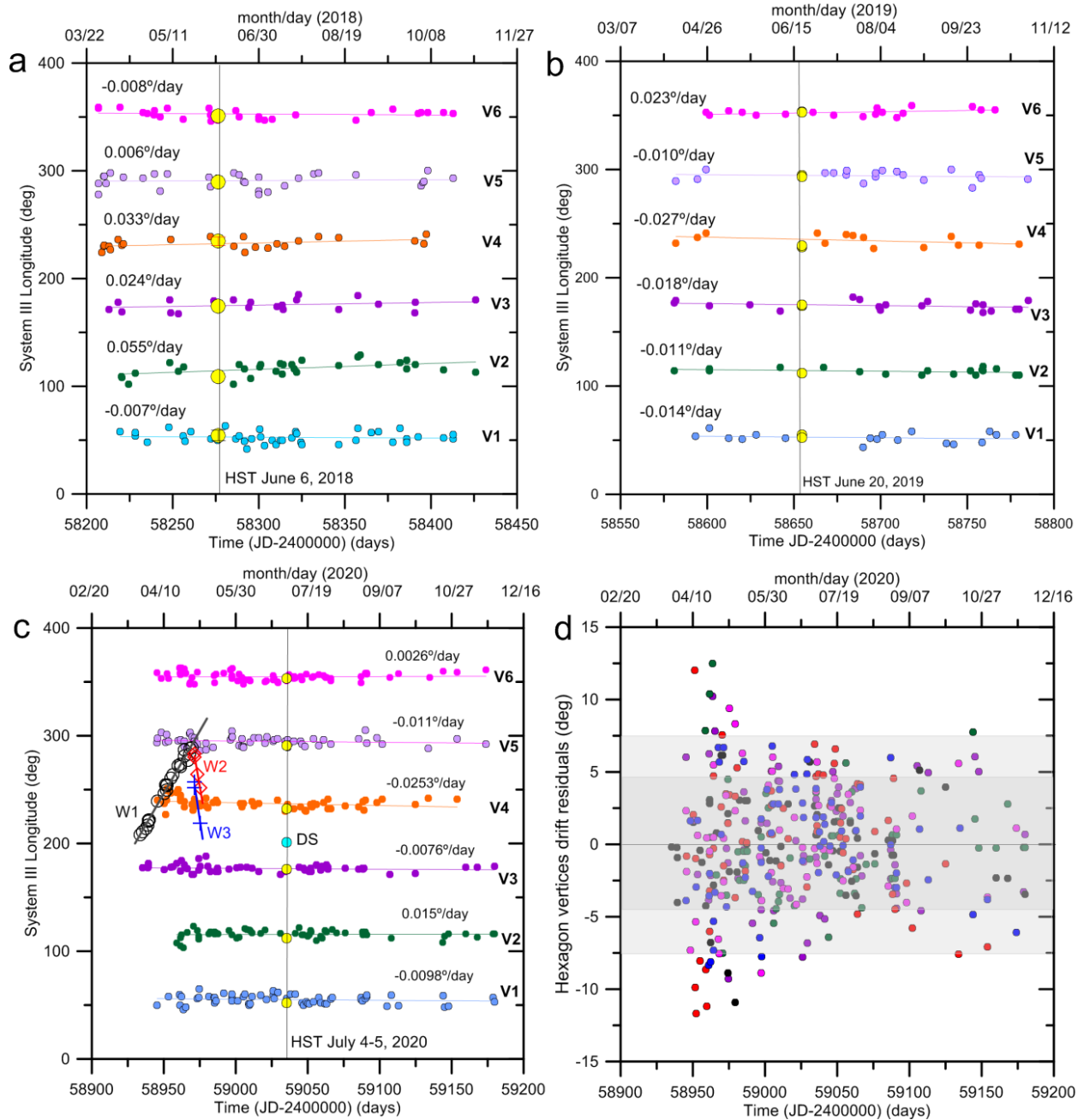
Figure 4. *System III longitudes of the vertices of the hexagon along 2018 (a), 2019 (b) and 2020 (c). Vertices identified V1 to V6 are indicated by different colors and yellow dots indicate measurements on HST images. Colored straight lines are linear fits to the position of each vertex, and the value of the drift rate (in degrees/day) is given above the fitted line. In (c) we include the tracks of the convective storms W1, W2, W3 as well as the position of the dark spot DS. (d) Plot of the residuals of the longitude position of the vertices in 2020 relative to the linear fits shown in (c).*

5. Numerical simulations of storms

We have used a parallelized version of the Shallow Water model (SW) developed by García-Melendo and Sánchez-Lavega (2017) to characterize the intensity of the 2020 storms. In our SW model, we try to reproduce the storm shape and evolution by changing the mass injection rate (Q) that mimics the convective source, its size, and source location on Saturn's wind profile. Details of the simulations are given in Supplementary Information). The SW model produces maps showing the evolution of a material tracer generated by the continuous injection of a mass flow during the whole simulation. In Figure 5 we show the result of a simulation that models the observed storm size and the formation and zonal expansion of an eastward wake. The material tracer is injected at latitude 76°N and the required mass flow is $Q = 5 \times 10^9$ m³s⁻¹. This value is similar to the value found for the 2018 storms ($Q = 2 \times 10^9$ m³s⁻¹) [Sánchez-Lavega et al., 2020] and in our preliminary analysis of the mid-latitude storms observed in the northern hemisphere during the Voyager 1 and 2 flybys [Smith et al., 1982; Sromovsky et al., 1983] and in the southern hemisphere with Cassini in 2004-2010 [Dyudina et al., 2007; Baines et al. 2009]. The intensity of all these storms is, however, much lower than the Great White Spots that appeared in 1960 at subpolar north latitudes ($Q = 10^{11}$ m³s⁻¹), in 1990 at equatorial latitudes ($Q = 10^{11}$-10^{12} m³s⁻¹) and in 2010 at north northern mid-latitude ($Q = 10^{10}$-10^{11} m³s⁻¹) [García-Melendo and Sánchez-Lavega, 2017; Sánchez-Lavega et al., 2018].
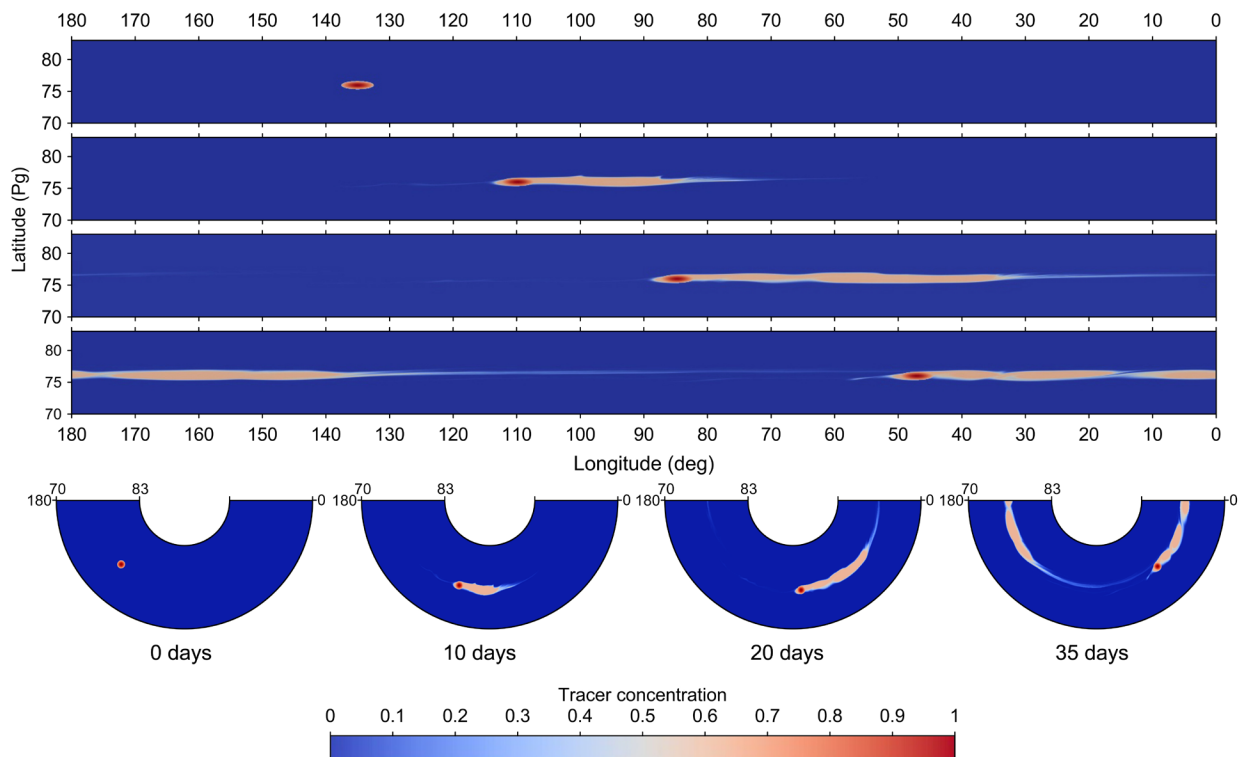
Figure 5. *Shallow Water numerical simulations of the convective storm evolution in Saturn's north polar wind field. The maps (upper cylindrical and lower polar projections) show the material tracer evolution in time for a continuous source with a mass flow $Q = 5 \times 10^9$ m³s⁻¹ and a size of 5 degrees*

254 *in longitude placed at latitude 76°S. Compare the upper map with figure 1a for the initial storm*
255 *aspect and the middle maps at 10 and 20 days with figures 1c and 1d for the eastward expansion*
256 *of the cloud.*

257
258

259 **6. Discussion and Conclusions**

260

261   The new convective storms reported here are the first observed at such high latitude in
262 Saturn. The storms in 2020 erupted at latitude 76.5°N, on the southern side of the hexagonal
263 wave. They appeared northward than those in 2018, thus we are tempted to propose that they
264 are a continuation of the activity that began that year at 67°N and spread north up to 75°N. Their
265 outbreak took place at Saturn's solar orbital longitude Ls = 121°-123° under high insolation at this
266 latitude (see Figure 6 in Sanchez-Lavega et al., 2020). The SW simulations of the size of the storms
267 and evolution indicate that they had comparable intensity to those of 2018, therefore suggesting
268 similar onset conditions in the region. The 2020 storms are also similar in their brightness, size
269 and tail formation, to a storm reported at high latitudes of the southern hemisphere [Sánchez-
270 Lavega et al., 1996].

271

272   The 2018-2020 storms are probably responsible for the changes we report on the cloud-
273 field albedo (the two belts and the bright zone) that delineate the hexagon. However, the
274 dynamics of the hexagonal wave do not appear to have been strongly affected by the storm
275 activity, the wave remaining robust in the face of these threats. This is in agreement with the fact
276 that we did not observe changes in the polar wind profile. The mean rotation period of the
277 hexagon in 2018-2020 was 10 h 39 min 21.1s ± 2.8 s (from Table 1). Since its discovery in 1980,
278 the rotation period of the hexagon [Sánchez-Lavega et al., 2014; Hueso et al., 2020] has perfectly
279 matched the radio-rotation period (10 h 39 min 22.4 s; System III) measured at the time of
280 Voyager 1 and 2 [Desch and Kaiser, 1981] and used by the IAU [Archinal et al., 2018]. Recent
281 estimates of the yet undetermined Saturn's rotation period, based on a combination of gravity-
282 field measurements, zonal wind measurements and radio-occultations [Anderson and Schubert,
283 2007], on dynamical grounds [Read et al., 2009] and on ring seismology [Mankovich et al., 2019]
284 propose a shorter period than system III, of the order of 10 h 33 min. If this were the case, the
285 wind profile velocity relative to the new system would shift to lower values, and the speed of the
286 hexagonal wave would be -22 ms^{-1} instead of ~ 0 ms^{-1}. This shift in the velocities does not affect
287 the Rossby wave model interpretation in Sánchez-Lavega et al. (2014).

288

289 The stability of the hexagon with respect to the nearby strong storms, together with its long
290 lifetime and survival to the strong seasonal insolation changes at its latitude, points towards a
291 meteorological formation with roots deep in Saturn's atmosphere, as proposed by some recent
292 models [Yadava and Bloxhama, 2020; Garcia et al., 2020]. This would be consistent with the deep
293 extension of the cloud top winds as deduced from gravity field measurements [Kaspi et al., 2020],
294 reinforcing the idea of its possible relationship with the bulk rotation of the planet [Sánchez-
295 Lavega, 2005; Sánchez-Lavega et al., 2014].

References

Anderson, J. D. and Schubert, G (2007). Saturn's gravitational field, internal rotation, and interior structure, *Science* 317, 1384-1387.

Antuñano, A., del Río-Gaztelurrutia T., Sánchez-Lavega A., and Hueso R. (2015). Dynamics of Saturn's polar regions, *J. Geophys. Res. Planets,* 120, 155–176, doi:10.1002/2014JE004709

Antuñano A., del Río-Gaztelurrutia T., Sánchez-Lavega A., Rodriguez Aseguinolaza J. (2018). Cloud Morphology and Dynamics in Saturn's Northern Polar Region, *Icarus,* 299, 117-132.

Archinal, B. A. et al. (2018) Report of the IAU working group on cartographic coordinates and rotation elements: 2015. *Celest. Mech. Dyn. Astr.* 130, 22.

Baines, K. H., Delitsky, M. L., Momary, Th. W., Brown, R. H. , Buratti, B. J., Clark, R. N., Nicholson P. D. (2009). Storm clouds on Saturn: Lightning-induced chemistry and associated materials consistet with Cassini/VIMS spectra, *Planet. Space Sci.,* 57, 1650-1658.

Cano, J. A. (1998) LAIA. Laboratorio de Análisis de Imágenes Astronómicas. Grup d'Estudis Astronomics, Barcelona. Accessed 2020 at http://www.ajax.ehu.es/Software/laia.html

del Río-Gaztelurrutia, T. et al. (2018). A planetary-scale disturbance in a long living three vortex coupled system in Saturn's atmosphere. *Icarus* **302**, 499–513.

Desch, M. D., and Kaiser L. M. (1981), Voyager measurements of the rotation period of Saturn's magnetic field, *Geophys. Res. Lett.,* 8, 253–256.

Dyudina, U.A., Ingersoll A.P., Ewald S.P., Porco C.C., Fischer G., Kurth W., Desch M., Del Genio A., Barbara J., and Ferrier J. (2007). Lightning storms on Saturn observed by Cassini ISS and RPWS during 2004-2006, *Icarus*, 190, 545-555. doi:10.1016/j.icarus.2007.03.035.

Garcia F., Chambers F. R. N. and Watts A. L. (2020). Deep model simulation of polar vortices in gas giant atmospheres, *Mont. Not. Roy. Astron. Soc.*, 499 (4), 4698–4715 doi.org/10.1093/mnras/staa2962

García-Melendo, E., Pérez-Hoyos S., Sánchez-Lavega A. and Hueso R. (2011). Saturn's zonal wind profile in 2004–2009 from Cassini ISS images and its long-term variability. *Icarus* 215, 62–74.

338 García-Melendo E., Hueso R., Sánchez-Lavega A., Legarreta J., del Rio-Gaztelurrutia T., Pérez-
339 Hoyos S. and Sanz-Requena J. F. (2013), Atmospheric dynamics of Saturn's 2010 giant storm,
340 *Nature Geoscience* 6, 525–529
341
342 García-Melendo, E. & Sánchez-Lavega, A. (2017). Shallow water simulations of Saturn's giant
343 storms at different latitudes, *Icarus* 286, 241–260
344
345 Hueso, R. & Sánchez-Lavega, A. (2004). A three-dimensional model of moist convection for the
346 giant planets II: Saturn's water and ammonia moist convective storms. *Icarus* 172, 255–271.
347
348 Hueso R., Legarreta J., García-Melendo E., Sánchez-Lavega A. & Pérez-Hoyos S. (2009). The Jovian
349 anticyclone BA: II. Circulation and models of its interaction with the zonal jets, *Icarus*, 203, 499-
350 515.
351
352 Hueso R., Juaristi J., Legarreta J., Sánchez-Lavega A., Rojas J. F., Erard S., Cecconi B., Le Sidaner P.
353 (2018), The Planetary Virtual Observatory and Laboratory (PVOL) and its integration into the
354 Virtual European Solar and Planetary Access (VESPA), *Planet. Space Sci.,* 150**,** 22-35.
355
356 Hueso R., Sanchez-Lavega A., Rojas J. F., Simon A., Barry T., de Rio-Gaztelurrutia T., Sayanagi K.M.,
357 Antuñano A., Blalock J., Colas F., Delcroix M., Gomez-Forrellad J. M., Gunnarson J., Peach D.,
358 Perez-Hoyos S., Wong M. H., (2020). Saturn atmospheric dynamics one year after Cassini: Long-
359 lived features and hexagon's drift rate variations, *Icarus*, 336, 113429*.*
360
361 Kaspi Y., Galanti E., Showman A. P., Stevenson D. J., Guillot T., Iess L. and Bolton S. J., (2020).
362 Comparison of the Deep Atmospheric Dynamics ofJupiter and Saturn in Light of the Juno and
363 Cassini Gravity Measurements, *Space Sci. Rev.*, 216:84. doi.org/10.1007/s11214-020-00705-7
364
365 Mankovich Ch., Marley M. S., Jonathan J. F., and Movshovitz, N. (2019). Cassini Ring Seismology
366 as a Probe of Saturn's Interior. I. Rigid Rotation, *Astrophys. J.,* 871:1 (15pp)
367
368 Morales-Juberías R., Sayanagi K. M., Simon A. A., Fletcher L. N., Cosentino R. G. (2015),
369 Meandering shallow atmospheric jet as a model of Saturn's North-Polar hexagon, *Astrophys. J.*
370 *Lett.*, 806, L18.
371
372 Read, P.L., Dowling, T. E. and Schubert, G. (2009). Saturn's rotation period from its atmospheric
373 planetary-wave configuration, *Nature* 460, 608-610.
374
375 Rostami M., Zeitlin V., Spiga A. (2017). On the dynamical nature of Saturn's North Polar hexagon,
376 *Icaru*s, 297, 59-70.
377
378 Sánchez Lavega, A., Lecacheux J., Gomez J. M., Colas F., Laques P., Noll K., Gilmore D., Miyazaki
379 I. & Parker D. (1996). Large-scale storms in Saturn's atmosphere during 1994. *Science* 271, 631–
380 634
381

382 Sánchez-Lavega, A., Rojas J. F., and Sada P. V. (2000), Saturn's zonal winds at cloud level, *Icarus*,
383 147, 405–420.

384

385 Sánchez-Lavega, A. (2005), How long is the day on Saturn? *Science*, 307, 1223–1224.

386

387 Sánchez-Lavega A., del Río-Gaztelurrutia T., Hueso R., Gómez-Forrellad J.M., Sanz-Requena J. F.,
388 Legarreta J., García-Melendo E., Colas F., Lecacheux J., Fletcher L. N., Barrado-Navascués D.,
389 Parker D. and the International Outer Planet Watch team (2011), Deep winds beneath Saturn's
390 upper clouds from a seasonal long-lived planetary-scale storm, *Nature,* 475, 71-74.

391

392 Sánchez-Lavega A., del Río-Gaztelurrutia T., Hueso R., Pérez-Hoyos S., García-Melendo E.,
393 Antuñano A., Mendikoa I., Rojas J. F., Lillo J., Barrado-Navascués D., Gomez-Forrellad J. M., Go C.,
394 Peach D., Barry T., Milika D. P., Nicholas P., and Wesley A. (2014). The long-term steady motion
395 of Saturn's hexagon and the stability of its enclosed jet stream under seasonal changes, *Geophys.*
396 *Res. Lett*., 41, 1425-1431.

397

398 Sánchez-Lavega A., Sromovsky L., Showman A., Del Genio A., Young R., Hueso R., García Melendo
399 E., Kaspi Y., Orton G. S., Barrado-Izagirre N., Choi D. & Barbara J., (2019). *Zonal Jets in Gas Giants*
400 chapter of the book *Zonal Jets*, pp. 9-45, eds. B. Galperin and P. Read, Cambridge University Press
401 (Cambridge, U.K.)

402

403 Sánchez-Lavega A., Fisher G., Fletcher L. N., Garcia-Melendo E., Hesman B., Perez-Hoyos S.,
404 Sayanagi K. & Sromovsky L., (2019). *The Great Storm of 2010-2011*, Chapter 13 of the book *Saturn*
405 *in the 21st Century*, pp. 377-416, eds. K. H. Baines, F. M. Flasar, N. Krupp, T. S. Stallard, Cambridge
406 University Press (Cambridge, U.K.)

407

408 Sánchez-Lavega, A., García-Melendo, E., Legarreta, J., Hueso, R., del Río-Gaztelurrutia, T., Sanz-
409 Requena, J. F., Pérez-Hoyos, S., Simon, A. A., Wong, M. H., Soria, M., Gómez-Forrellad, J. M.,
410 Barry, T., Delcroix, M., Sayanagi, K. M., Blalock, J. J., Gunnarson, J. L., Dyudina, U., Ewald, S., 2020.
411 A complex storm system in Saturn's north polar atmosphere in 2018. Nature Astronomy 4, 180-
412 187. Doi: 10.1038/s41550-019-0914-9.

413

414 Sanz-Requena, J. F., Pérez-Hoyos S., Sánchez-Lavega A., Antuñano A. & Irwin P. J. (2018). Haze
415 and cloud structure of Saturn's North Pole and Hexagon Wave from Cassini/ISS imaging. *Icarus*
416 305, 284–300.

417

418 Sayanagi, K., Baines, K., Dyudina, U., Fletcher, L., Sánchez-Lavega, A., & West, R. (2019). Saturn's
419 Polar Atmosphere, in *Saturn in the 21st Century*, pp. 337-376, K. Baines, F. Flasar, N. Krupp, & T.
420 Stallard (Eds.), Cambridge University Press (Cambridge, U. K.)

421

422 Simon A. A , Wong M. H and Orton G.S. (2015). First results from the Hubble OPAL program:
423 Jupiter in 2015, *Astrophys. J. Lett*., 812, 55.

424

425   Simon A. A., Hueso R., Sánchez-Lavega A., Wong M. H. (2021). Mid-summer atmospheric changes
426   in Saturn's northern hemisphere from the Hubble OPAL program, *Planet. Sci. J.,* <mark>2:47 (9pp)</mark>
427
428   Smith, B. A., Soderblom, L., Batson, R. M., Bridges, P. M., Inge, J. L., Masursky, H., Shoemaker, E.,
429   Beebe, R. F., Boyce, J., Briggs, G., Bunker, A., Collins, S. A., Hansen, C., Johnson, T. V., Mitchell, J.
430   L., Terrile, R. J., Cook, A. F., Cuzzi, J. N., Pollack, J. B., Danielson, G. E., Ingersoll, A. P., Davies, M.
431   E., Hunt, G. E., Morrison, D., Owen, T., Sagan, C., Veverka, J., Strom, R., and Suomi, V. E. (1982).
432   A new look at the Saturn system - The Voyager 2 images. *Science*, 215, 504-537.
433
434   Sromovsky, L. A., Revercomb H. E., Krauss R. J., & Suomi V. E. (1983). Voyager 2 observations of
435   Saturn's northern mid-latitude cloud features: morphology, motions, and evolution, *J. Geophys.*
436   *Res.* 88, 8650–8666
437
438   Yadava R. K. & Bloxhama J. (2020), Deep rotating convection generates the polar hexagon on
439   Saturn, *Proc. Nat. Acad. Sci.*, 117, 13991-13996. doi:10.1073/pnas.2000317117

440

441 **Acknowledgments**

442

456

457

458 **Data availability**

459

460 The data that support the plots within this paper and other findings of this study are available at
461 the following repository (private access for editor and reviewers for evaluation):
462 https://figshare.com/s/f39fcf055d3337997a01
463 https://doi.org/10.6084/m9.figshare.13546793
464 The ground-based images included in the above repository have been downloaded from the
465 following sources:
466 Association of Lunar and Planetary Observers ALPO – Japan:
467 http://alpo-j.sakura.ne.jp/Latest/Jupiter.htm
468 PVOL2 database: http://pvol2.ehu.eus/pvol2/

469   Images from the HST-OPAL program are available at:

470   https://archive.stsci.edu/prepds/opal/

471   The image navigation software WinJupos is available at:

472   http://jupos.org/gh/download.htm

473   The image correlation software PICV can be accessed at:

474   https://doi.org/10.5281/zenodo.4312675

475   The shallow water model code can be accessed at:

476   https://doi.org/10.5281/zenodo.4312681